Optimal Design and Experimental Assessment of a Wireless Power Transfer System for Home-Cage Monitoring

Jeff Po-Wa Chow, *Member, IEEE*, Henry Shu-Hung Chung, *Fellow, IEEE*, Leanne Lai-Hang Chan, *Senior Member, IEEE*, Ruihua Shen, and Sai Chun Tang, *Senior Member, IEEE*

***Abstract*—Techniques of long-term *in vivo* electrophysiological recording play important roles in brain research and neural rehabilitation. To avoid interruption of experiment and risk of infection, use of wireless power transfer (WPT) technique has been suggested to eliminate cumbersome wires and batteries attached to the animals in rodent electrophysiological applications. This paper presents a holistic assessment of the relationships among the physical sizes of the transmitting and receiving coils, power transfer characteristics, and specific absorption rate (SAR) in animals of a simple WPT system using two rectangular coaxial transmitting coils. With given space for the animal and size of the receiving coil, a procedure for designing the minimum driving current, and the transmitting coil dimensions and separation to deliver sufficient power to the receiver, and interactions between the transmitting and receiving coils is derived. A π-capacitor network that can match the impedances of the receiving coil and the load to operate the receiver at the maximum power transfer condition is proposed. It is also optimized for the overall volume. A 100-mW prototype with an operating zone of $400 \times 240 \times 40$ mm^3 and a receiving coil with a diameter of 11.45 mm is built and studied. The SAR in the animal is evaluated and compared with the recommended restriction level.**

***Index Terms*—Electrophysiological experiments, impedance matching circuit, magnetic flux density, specific absorption rate (SAR), wireless power transfer (WPT).**

I. Introduction

TECHNIQUES of long-term *in vivo* electrophysiological recording play important roles in brain research and neural rehabilitation, such as deep brain stimulation and treatment

Manuscript received June 9, 2018; revised August 21, 2018 and November 21, 2018; accepted January 4, 2019. Date of publication January 21, 2019; date of current version June 28, 2019. This work was supported by the Research Grants Council of the Hong Kong Special Administrative Region, China, through Project CityU 112613. This paper was presented in part at the IEEE Energy Conversion Congress and Exposition 2017. The paper was awarded the best paper award by the Technical Committee on High-Performance and Emerging Technologies, IEEE Power Electronics Society, at ECCE 2018. Recommended for publication by Associate Editor F. Costa. *(Corresponding author: Henry Shu-Hung Chung.)*

The authors are with the Centre for Smart Energy Conversion and Utilization Research, Department of Electronic Engineering City University of Hong Kong, Kowloon, Hong Kong (e-mail:

Efforts on simplifying the system have been made. In [10] and [19], the position tracking system is eliminated by connecting all resonator coils in parallel. The transmitting coil delivers power to the receiver through the resonator coils, close to the receiving coil physically. However, the power losses will increase with the number of coils in the array as all the coils in parallel connection are concurrently energized. The SAR has not been fully evaluated.

The design of transmitting coil has also attracted a lot of attention to achieve a simple system, [16], [20]–[23]. In [16], the inductive link was implemented by using a single, large transmitting coil to produce a magnetic field in the cage. However, as reported in [8] and [24], such a large coil causes self-resonance at low frequency. A single transmitting coil mounted on a mechanical *XY* moving table has been proposed in [20]. By using a permanent magnet to keep tracking the position of the receiver, the transmitting coil is moved to a location close to the receiving coil. However, the fast-moving mechanical parts could produce unwanted acoustic noise and vibration, adversely affecting the animal behavior [25]. WPT systems with large columnar- and planar-shaped resonating coils have been presented and compared in [21]. The columnar-shaped resonating coils can generate a relatively uniform magnetic flux for the receiver. One of the main challenges is their bulk sizes, which limit the flexibility in the coil optimization. Multiple coils with different orientations have been implemented in the inductive link to minimize the sensitivity of coil misalignment by authors in [22] and [23]. Intelligent tracking systems and high-performance feedback subsystems are required and will lead to a more complicated system.

A WPT system without dedicated position tracking circuit or feedback control systems is proposed. The transmitting coil comprises two large coaxial rectangular windings to produce magnetic flux density with allowable fluctuations. The transmitting coil is divided into multiple segments with resonant capacitors to reduce the voltage over the transmitting coil to a safer level and eliminate self-resonance [24], [26]. A holistic assessment of the relationships among the physical sizes of the coils, power transfer characteristics, interactions between transmitting and receiving coils, is conducted. Moreover, a π-capacitor matching circuit that can match the receiving coil and the load is designed to operate the receiver at the maximum power transfer condition and minimize the transmitting coil current as well as the SAR in animal tissues. The matching circuit is also optimized for the overall volume. A 100-mW prototype is built and studied. Finally, the SAR in the animal is evaluated and compared with the recommended restriction level.

II. Overview of the Proposed System

Several practical considerations should be taken into account. First, the system should be simple and low cost, and does not block the line of sight to observe animal activities. Second, the receiver can receive sufficient power from the transmitter, even if the animal is moving rapidly in the cage. Third, the SAR in animal must be lower than the limit recommended by some international safety standards [27], aiming to protect the body from adverse heating effect under exposures to electromagnetic fields. The recommended basic restriction (BR) is protective against tissue temperature increases of more than a small fraction of 1 °C. As discussed in [9], the allowable SAR level for rodents should be five times lower than the recommended limit for humans, as small animals have a less effective thermoregulatory system [28]–[30].

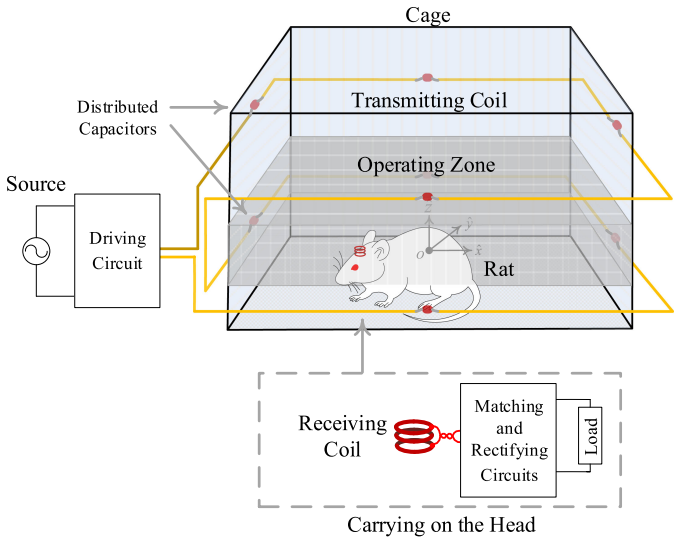

Fig. 1. Configuration of the proposed WPT system.

Fig. 1 shows the proposed transmitting coil. It is composed of two series-connected coaxial rectangular windings: one upper and one lower. The cage is placed inside the coil. Its shape is rectangular, instead of square, as the animal would feel more secure [25]. The receiver is carried by the head of the animal. The operating zone for the receiving coil is defined within the cage. It has the same footprint as the cage and the same height as the receiver carried by the animals. To avoid the coil from blocking line of sight, the thickness of each winding should be kept small.

Fig. 2 shows the equivalent circuit. The coupling between the transmitting and receiving coils is represented by a transformer model [31]. $v_{\rm in}$ and $i_{\rm in}$ denote the transmitter input voltage and transmitting coil current in an rms value, respectively. The voltages induced in the transmitting and receiving coils are denoted by ε_1 and ε_2, respectively. The self-inductances and winding resistances of the transmitting and receiving coils are L_1, L_2, r_1, and r_2, respectively. C_1 represents the equivalent capacitance of the series resonant capacitors distributed over the capacitor-segmented transmitting coil. Such technique can reduce the operating coil voltage to a safer level [24], [26]. The transmitting coil is tuned to the operating frequency by adjusting C_1 to maximize power transfer. A π-type impedance matching circuit, formed by C_{21}, C_{22}, and C_{23}, is connected between the receiving coil and the diode-bridge rectifier to maximize the power received. Thus, the transmitting coil current and SAR are minimized. The output voltage of the impedance matching

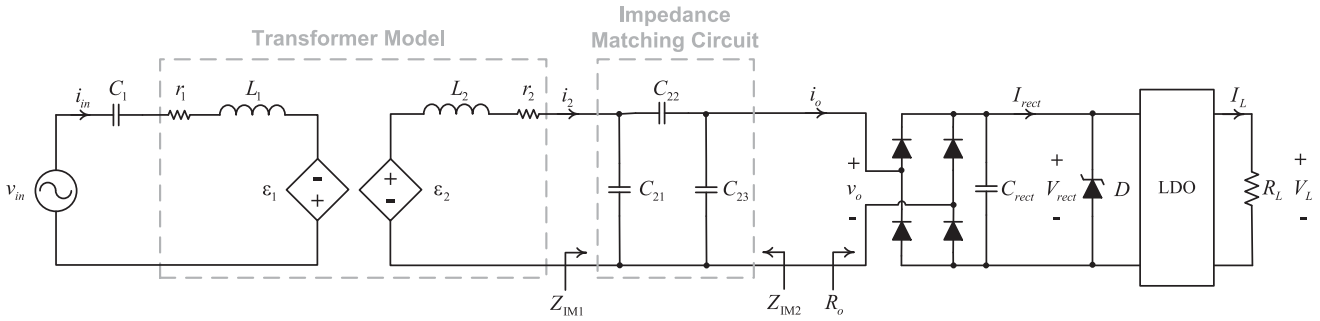

Fig. 2. Equivalent circuit of the WPT system.

circuit, v_o, is rectified by a diode bridge and stabilized by a ceramic capacitor and a supercapacitor to avoid power interruption, due to coil misalignment. The total capacitance of the two capacitors is $C_{\rm rect}$. The rectified average voltage and current are denoted by $V_{\rm rect}$ and $I_{\rm rect}$, respectively. A zener diode, *D*, is added to protect the supercapacitor from overvoltage. A low-dropout (LDO) regulator is used to regulate the load voltage V_L. I_L represents the load current.

When an animal walks or rests in the cage, the receiving coil placed on the animal's head is practically parallel to the transmitting coil. When it climbs and leans on the cage wall, the receiving coil is almost perpendicular to the transmitting coil and the power transfer will be affected. As discussed in [32], the duration of power interruption is usually less than 5 s. This issue can be solved by adding a supercapacitor or a low-capacity rechargeable miniature battery [33], in the receiver to maintain the load power [9], [10], [17], [18]. Alternatively, the coil structures with different oriented windings can be used to stabilize the output power when angular coil misalignment occurs [22], [23], [34], [35]. For the sake of simplicity, a supercapacitor is used. The chosen value of the supercapacitor in the prototype is designed to sustain load power for around 5 s. Thus, the current design can deal with majority of events. Nevertheless, the time duration can be lengthened by further increasing the value of the capacitor.

III. Impedance Matching Circuit for Achieving Maximum Output Power

As the receiving coil is much smaller than the transmitting coil, the coupling coefficient is small. The input impedance and generated magnetic field pattern are not noticeably affected by the loading condition on the receiver side. The effects of the nonlinear characteristic of the diode-bridge rectifier on the input impedance, as reported in [31], become insignificant.

A. Allowable Ranges of P_o and R_o

The equivalent output impedance of the link is modeled by R_o. The output power of the link is P_o. Assuming that the input voltage of the LDO, $V_{\rm rect}$, is allowed to vary between $V_{\rm rect,min}$ and $V_{\rm rect,max}$, the minimum and maximum values of P_o are

$$P_{o,\min} = (V_{\rm rect,min} + 2V_f)\frac{P_L}{V_L} \tag{1a}$$

$$P_{o,\max} = (V_{\rm rect,max} + 2V_f)\frac{P_L}{V_L} \tag{1b}$$

where V_f is the total forward diode voltage drop in the bridge, P_L is the maximum load power, and V_L is the load voltage.

The equivalent output resistance, R_o, which varies between $R_{o,\min}$ and $R_{o,\max}$, is [37]

$$R_{o,\min} = \frac{8V_L}{\pi^2}\left(\frac{V_{\rm rect,min} + 2V_f}{P_L}\right) \tag{2a}$$

$$R_{o,\max} = \frac{8V_L}{\pi^2}\left(\frac{V_{\rm rect,max} + 2V_f}{P_L}\right). \tag{2b}$$

B. Maximum Power Transfer Condition on the Receiver

With the same output power, operating the system at the maximum power transfer condition requires lower transmitting coil current than that at the maximum efficiency condition. The generated magnetic flux density is reduced by decreasing the transmitting coil current. It is thus preferable to operate the system at the maximum power transfer condition to minimize the SAR. Although the system is not operated at the maximum efficiency, the power losses in the coils do not cause noticeable temperature rise in the coils and cage, as the power level of this kind of applications is low, typically less than 100 mW [8]–[10], [16]–[21].

Fig. 2 shows a matching circuit. Its input impedance $Z_{\rm IM1}$ and output impedance $Z_{\rm IM2}$ are

$$Z_{\rm IM1} = \frac{X_{C21}[X_{C22}X_{C23} + R_o(X_{C22} + X_{C23})]}{X_{C23}(X_{C21} + X_{C22}) + R_o(X_{C21} + X_{C22} + X_{C23})} \tag{3}$$

$$Z_{\rm IM2} = \frac{X_{C23}[X_{C22}Z_2 + X_{C21}(X_{C22} + Z_2)]}{Z_2(X_{C22} + X_{C23}) + X_{C21}(X_{C22} + X_{C23} + Z_2)} \tag{4}$$

where $X_{C21} = \frac{1}{j\omega C_{21}}$, $X_{C22} = \frac{1}{j\omega C_{22}}$, $X_{C23} = \frac{1}{j\omega C_{23}}$, and $Z_2 = r_2 + j\,\omega\,L_2$.

The circuit is designed to receive sufficient power from the transmitter under the worst-case situation, where $R_o = R_{o,\min}$.

TABLE I
DIFFERENT COMBINATIONS OF CAPACITORS FOR THE IMPEDANCE MATCHING CIRCUIT

$\hat{C}_{21}$	C_{21} (nF)	C_{22} (nF)	C_{23} (nF)	$C_{2,\text{sum}}$ (nF)	Size† (mm^3)
1.000	**3.49***	**0.13**	**0.00**	**3.62**	**130.0**
0.997	3.47	0.16	0.21	3.84	153.0
0.800	2.79	1.10	3.25	7.14	263.8
0.600	2.09	2.02	6.06	10.17	308.0
0.400	1.39	2.95	8.85	13.19	425.5
0.200	0.70	3.88	11.65	16.23	467.1
0.000	0.00	4.81	14.43	19.24	536.0

*Assuming that $C_{21} = 3.49\,\text{nF}$, when $\hat{C}_{21} = 1$.
†Total volume occupied by the capacitors C_{21}, C_{22}, and C_{23} [38].

Then, based on (3) and (4), the matching conditions are

$$\frac{X_{C21}[X_{C22}X_{C23} + R_{o,\min}(X_{C22} + X_{C23})]}{X_{C23}(X_{C21} + X_{C22}) + R_{o,\min}(X_{C21} + X_{C22} + X_{C23})} = r_2 - j\omega L_2 \tag{5}$$

$$\frac{X_{C23}[X_{C22}Z_2 + X_{C21}(X_{C22} + Z_2)]}{Z_2(X_{C22} + X_{C23}) + X_{C21}(X_{C22} + X_{C23} + Z_2)} = R_{o,\min}. \tag{6}$$

For a given value of C_{21}

$$C_{22} = \frac{1}{\omega}\frac{\omega L_2 - \omega C_{21}({r_2}^2 + \omega^2 {L_2}^2) + \sqrt{G}}{r_2(r_2 - R_{o,\min}) + \omega^2 {L_2}^2} \tag{7}$$

$$C_{23} = \frac{1}{\omega}\frac{\sqrt{G}}{r_2 R_{o,\min}} \tag{8}$$

where $G = {r_2}^2(\omega^2 {C_{21}}^2 r_2 R_{o,\min} - 1) + r_2 R_{o,\min}(\omega^2 L_2 C_{21} - 1)^2$.

In order to ensure that C_{22} and $C_{23} \geq 0$, the following condition should be satisfied:

$$C_{21} \leq \frac{\omega L_2 R_{o,\min} - \sqrt{r_2 R_{o,\min}({r_2}^2 - r_2 R_{o,\min} + \omega^2 {L_2}^2)}}{\omega R_{o,\min}({r_2}^2 + \omega^2 {L_2}^2)}. \tag{9}$$

C. Minimization of the Size of the Impedance Matching Circuit

The total capacitor volumes with different combinations of C_{21}, C_{22}, and C_{23} are compared. Let $C_{2,\text{sum}}$ be the sum of the capacitance values

$$C_{2,\text{sum}} = C_{21} + C_{22} + C_{23}. \tag{10}$$

Let $\hat{C}_{21}$ be normalized C_{21} by the value defined on the RHS of (9). Table I shows the values of $C_{2,\text{sum}}$ and the total volume occupied with different values of $\hat{C}_{21}$. The values of C_{22} and C_{23} are determined by using (7) and (8), respectively. The capacitors are of mica type [38].

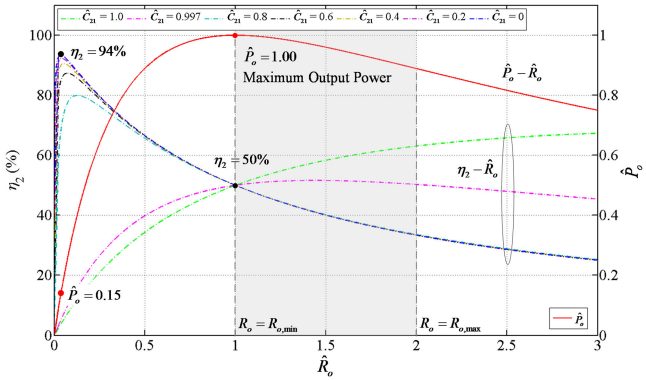

Fig. 3. $\eta_2 - \hat{R}_o$ and $\hat{P}_o - \hat{R}_o$ for π-capacitor impedance matching circuit.

D. Maintaining the Power Efficiency of the Receiver Side Over 50%

In practice, $R_o \in [R_{o,\min}, R_{o,\max}]$. Let $\hat{R}_o$ be the normalized value. Mathematically

$$\hat{R}_o = \frac{R_o}{R_{o,\min}}. \tag{11}$$

The output power of the link and the power efficiency of the receiver side, η_2, are

$$P_o = \frac{\hat{R}_o}{(1 + \hat{R}_o)^2}\frac{|\varepsilon_2|^2}{2r_2} \tag{12}$$

$$\eta_2 = \frac{P_o}{P_o + P_{\text{loss2}}} \tag{13}$$

where P_{loss2} is the power loss of the receiving coil, i.e., $P_{\text{loss2}} = |i_2|^2 r_2/2$. i_2 is the receiving coil current. It should be noted that η_2 does not include the power loss of the transmitting coil.

Fig. 3 shows a family of normalized output power $\hat{P}_o$ and efficiency η_2 versus $\hat{R}_o$ under different values of $\hat{C}_{21}$ and with the same transmitting coil current. Since the circuit is operated at the matched condition, the curve $\hat{P}_o$–$\hat{R}_o$ is independent of $\hat{C}_{21}$. However, the efficiency curve η_2–$\hat{R}_o$ varies with $\hat{C}_{21}$. In order to maintain the efficiency no less than 50% over the designed load range, i.e., $\hat{C}_{21} > 0.997$. By combining the analysis of

Section III-C and D, $\hat{C}_{21}$ is chosen to be equal to unity in the following discussion, and then C_{23} is equal to zero.

IV. Design and Optimization of the Inductive Link

A. Optimization of the Receiving Coil

The dimensions of the receiving coil are strictly limited by the rodent electrophysiological application and set as $11.5 \times 6 \times 6$ mm^3. A single-layer helical coil is used in the receiver side. The coil self-inductance, L_2, coil resistance, r_2, and quality factor, Q_2, can be expressed as

$$L_2 = \mu_0 N_2 \left[\ln\left(\frac{8d_r}{d_w}\right) - 1.75\right] + \frac{\mu_0 d_r}{2}\left[\sum_{i=1}^{N_2}\sum_{j=1}^{N_2}\left[\left(\frac{2}{k_c} - k_c\right)K(k_c) - \frac{2}{k_c}E(k_c)\right](1-\psi_{ij})\right] - \frac{\mu_0 N_2 d_r}{2}(k_s + k_m) \tag{14}$$

$$r_2 = \frac{4N_2 d_r}{{d_w}^2 \sigma_{\mathrm{Cu}}}\Phi_{\mathrm{cond}}\left(\frac{d_w}{2\delta}\right) + \frac{4\pi^2 d_r}{\sigma_{\mathrm{Cu}}}\Phi_{\mathrm{ind}}\left(\frac{d_w}{2\delta}\right)\sum_{p=1}^{N_2}\langle {H_p}^2\rangle \tag{15}$$

$$Q_2 = \frac{\omega L_2}{r_2} \tag{16}$$

where $\omega = 2\pi f$, μ_0 is the permeability of vacuum, N_2 is the number of turns, and d_w is the circular wire diameters. L_2 and r_2 are presented in [39]–[42]. Rosa's inductance correction coefficients [40] have been applied to the coil inductance calculation in (14) to improve the accuracy. The expressions of the parameters are given in Appendix A.

Fig. 4 shows a family of Q_2 and L_2 versus N_2 under different values of d_w. For the sake of comparison, the coils are kept at the same outer dimension by adjusting the coil diameters and winding separations. The results are calculated by (14)–(16) and simulated with COMSOL Multiphysics [43]. As d_w and N_2 increase, Q_2 increases and L_2 decreases. However, when L_2 is too small, the required $C_{2,\mathrm{sum}}$ and the size of the impedance matching circuit become too large and oversized. Thus, it is practically infeasible. In this design, $N_2 = 4$ is chosen to maintain the value of L_2 to be larger than 100 nH and $d_w = 1.3\,\mathrm{mm}$ is selected to maximize the value of Q_2.

B. Allowable Range and Variation of B_z

The rat has mostly its four limbs stepped on the cage, so the transmitting and receiving coils are oriented in parallel. Therefore, only the z-component of the magnetic flux density is considered. Based on the ranges of P_o and R_o in (1) and (2), the minimum and maximum values of the z-component of the magnetic flux density, $B_{z,\min}$ and $B_{z,\max}$, respectively, are

$$B_{z,\min} = \frac{\sqrt{R_{o,\min}P_{o,\min}}}{\omega N_2 A_2}\left|\frac{(R_{o,\min}+X_{C22})(Z_{\mathrm{IM1,min}}+Z_2)}{R_{o,\min}Z_{\mathrm{IM1,min}}}\right| \tag{17a}$$

$$B_{z,\max} = \frac{\sqrt{R_{o,\max}P_{o,\max}}}{\omega N_2 A_2}\left|\frac{(R_{o,\max}+X_{C22})(Z_{\mathrm{IM1,max}}+Z_2)}{R_{o,\max}Z_{\mathrm{IM1,max}}}\right| \tag{17b}$$

where $Z_{\mathrm{IM1,min}} = \frac{X_{C21}(X_{C22}+R_{o,\min})}{X_{C21}+X_{C22}+R_{o,\min}}$ and $Z_{\mathrm{IM1,max}} = \frac{X_{C21}(X_{C22}+R_{o,\max})}{X_{C21}+X_{C22}+R_{o,\max}}$.

Let ΔB_z be the variation of B_z

$$\Delta B_z = \frac{B_{z,\max} - B_{z,\min}}{B_{z,\min}}. \tag{18}$$

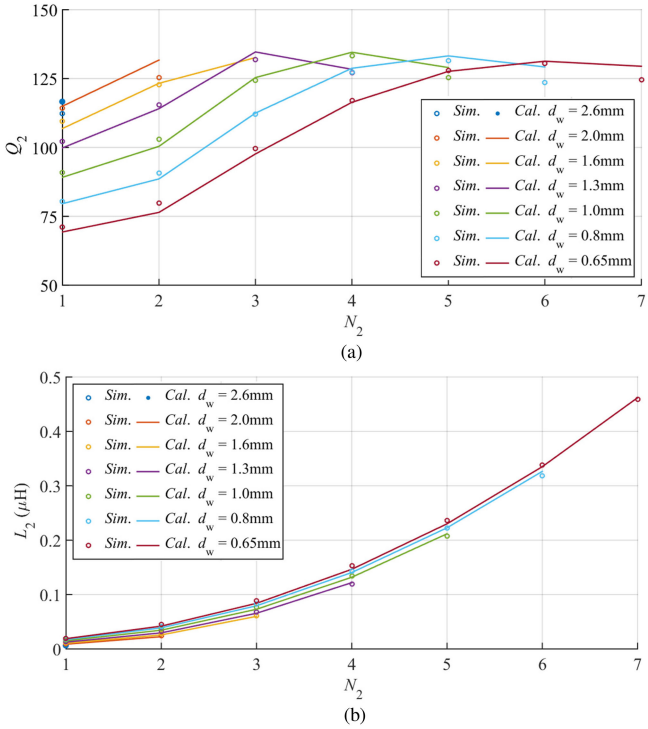

Fig. 4. $Q_2 - N_2$ and $L_2 - N_2$ under different d_w and with the same outer coil dimension ($11.5 \times 6 \times 6$ mm^3). (a) Quality factor. (b) Self-inductance.

C. Optimization of the Transmitting Coil

Commercially available cages for rodent animals [44], [45] are selected. The dimensions are $400 \times 240 \times 200$ mm^3. The operating zone has the same footprint as the cage and the height to cover the vertical movement of the receiver while the animal is walking and standing [8]–[10], [17]–[21]. The operating zone is $400 \times 240 \times 40$ mm^3. The Cartesian coordinate system is defined in Fig. 5. The centers of the operating zone and the transmitting coil are the same and defined as the origin. The center of the operating zone is 70 mm above the floor of the cage. The dimensions of the upper and lower windings are the

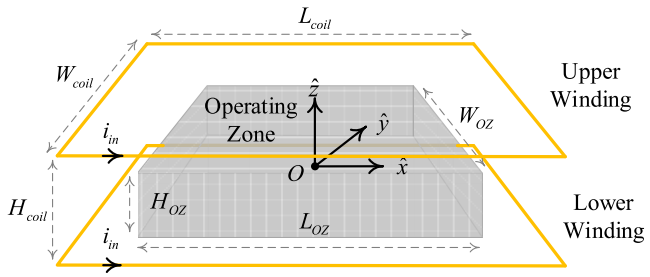

Fig. 5. Setup of transmitting coil and operating zone.

same. The coil length and width are denoted by L_{coil} and W_{coil}, respectively. The coil separation is denoted by H_{coil}. The length, width, and height of the operating zone are denoted by L_{OZ}, W_{OZ}, and H_{OZ}, respectively.

The transmitting coil is designed to provide the same or lower variation of the magnetic flux density within the operating zone (see Section IV-C). The dimensions and separation of the two windings are minimized. The variation of the magnetic flux density is calculated numerically. To generalize the analysis of the generated magnetic field, the dimensions of the operating zone are normalized by the transmitting coil and three ratios, LR, WR, and HR, are defined as

$$\text{LR} = \frac{L_{OZ}}{L_{\text{coil}}} \tag{19a}$$

$$\text{WR} = \frac{W_{OZ}}{W_{\text{coil}}} \tag{19b}$$

$$\text{HR} = \frac{H_{OZ}}{H_{\text{coil}}}. \tag{19c}$$

Since $L_{OZ} < L_{\text{coil}}$, $W_{OZ} < W_{\text{coil}}$, and $H_{OZ} < H_{\text{coil}}$, LR, WR, and HR all are less than 1. To simplify the analysis, the footprints of the operating zone and the coil have the same aspect ratios. Thus

$$\text{WR} = \text{LR}. \tag{20}$$

The ratio of the footprint areas between the operating zone and the coil, AR, is given by

$$\text{AR} = \text{LR}^2. \tag{21}$$

The z-component of the magnetic flux density at (x, y, z) [46] generated by the upper and lower windings, B_{1z} and B_{2z}, respectively, is

$$B_{1z}(x,y,z) = \frac{\mu_0 i_{\text{in}}}{4\pi L_{\text{coil}}} \sum_{k=1}^{4} \frac{(-1)^k g_k}{\delta_{1k}[\delta_{1k} + (-1)^{(k+1)} e_k]} - \frac{e_k}{\delta_{1k}(\delta_{1k} + g_k)} \tag{22a}$$

$$B_{2z}(x,y,z) = \frac{\mu_0 i_{\text{in}}}{4\pi L_{\text{coil}}} \sum_{k=1}^{4} \frac{(-1)^k g_k}{\delta_{2k}[\delta_{2k} + (-1)^{(k+1)} e_k]} - \frac{e_k}{\delta_{2k}(\delta_{2k} + g_k)} \tag{22b}$$

where g_k, e_k, δ_{1k}, and δ_{2k} are given in Appendix B.

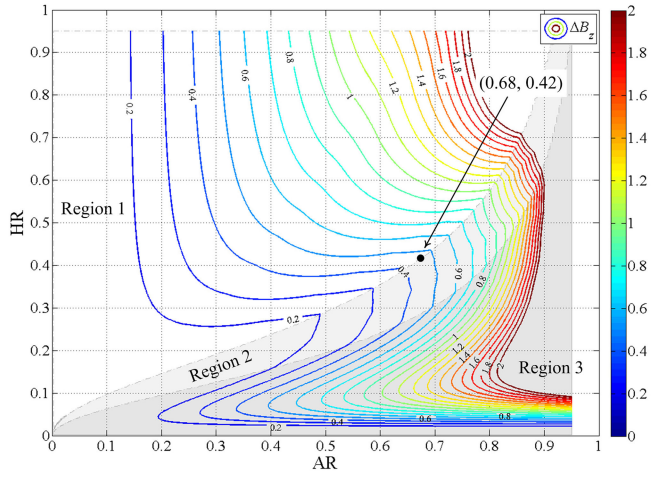

Fig. 6. ΔB_z and position for $B_{1A,\min}$ versus HR and AR. ($L_{OZ} \times W_{OZ} \times H_{OZ} = 400 \times 240 \times 40$ mm^3)

The z-component of the resultant magnetic flux density B_z is obtained by B_{1z} and B_{2z}

$$B_z(x,y,z) = B_{1z}(x,y,z) + B_{2z}(x,y,z). \tag{23}$$

Since the transmitting coil and the operating zone are concentric and symmetric about the x-, y-, and z-axes, the profile of B_z is symmetric and only B_z in the positive coordinates is needed. The ranges of the Cartesian coordinates are confined by the dimensions of the operating zone, i.e.,$x \in [0, L_{OZ}/2]$, $y \in [0, W_{OZ}/2]$, and $z \in [0, H_{OZ}/2]$.

B_z at each point is calculated by using (11) and (13) with $i_{\text{in}} = 1$ A. The minimum and maximum values of B_z are determined by a numerical approach and expressed as

$$B_{1\text{A,min}} = \arg\min_{x,y,z} B_z(x,y,z) \tag{24a}$$

$$B_{1A,\max} = \arg\max_{x,y,z} B_z(x,y,z). \tag{24b}$$

ΔB_z is calculated by (18) and (24a) and (24b). Fig. 6 shows the contour lines with ΔB_z under different AR and HR. The contours with ΔB_z for four normalized operating zones are presented in [36].

The geometric parameters, AR and HR, with respect to the coil dimensions can be determined, while the variation of the magnetic flux density, ΔB_z, can be confined within the designed allowable variation in Section IV-C. The transmitting coil size and separation are minimized by maximizing AR and HR. The combinations of AR and HR are chosen to be the tip of the curve with AR maximum, as marked in Fig. 6. L_{coil}, W_{coil}, and H_{coil} are calculated by solving (19a), (19b), (19c)–(21).

D. Transmitting Coil Current

The rms value of the transmitting coil current, i_{in}, is thus determined by

$$i_{\text{in}} = \frac{B_{z,\min}}{N_1 B_{1\text{A,min}}} \tag{25}$$

TABLE II
COORDINATES OF $B_{1A,\min}$ AT REGIONS 1–3 IN FIG. 6

Region	Coordinates for $B_{1A,\min}$		
	x	y	z
1	0	0	$H_{OZ}/2$
2	0	$W_{OZ}/2$	0
3	$L_{OZ}/2$	$W_{OZ}/2$	0

where N_1 is the number of turns of the upper/lower winding in the transmitting coil, and $B_{z,\min}$ is determined by (17a).

Fig. 6 shows the regions of the corresponding position of $B_{1A,\min}$ with different ΔB_z, AR, and HR. The coordinates of the positions are given in Table II. $B_{1A,\min}$ can be obtained by substituting the coordinates and the coil dimensions into (22a), (22b), and (23).

V. EXPERIMENTAL PROTOTYPE

The performances of the WPT system are verified and evaluated on a prototype shown in Fig. 7. The circuit schematic is shown in Fig. 2. The design specifications are shown in Table III. The system design is based on the considerations described in Sections III and IV. A transmitting coil with two turns, one for the upper winding and one for the lower winding, is designed. It is shown in Fig. 7(a). The centers of the operating zone and the transmitting coil are the same and 70 mm above the floor of the cage. The parameters and component values are tabulated in Table IV. Each winding is divided into four segments and each segment is connected to another segment through a capacitor, so as to reduce the coil voltage [24], [26] by canceling the effect of the self-inductance of each segment of the transmitting coil. The operating frequency is set to 6.78 MHz, within the industrial, scientific, and medical radio band. The details of the driver design have been presented in [36]. A prototype receiver, shown in Fig. 7(b), is built and the component values are given in Table V. The dimensions of the entire receiver are $24.5 \times 13 \times 16$ mm^3. The electrical parameters of the coil are measured by an impedance analyzer (Hewlett Packard 4194A).

A. Comparison on the Theoretical and Measured Magnetic Flux Density

Fig. 8 shows the contour lines of B_z, calculated by (22a), (22b), and (23), on the *XY* plane at $z = 0$. i_{in} equals 2 A. The shaded regions indicate the operating zone. The transmitting coil generates a uniform magnetic flux profile within the operating zone. The coil dimensions are optimized. The contour line density is significantly increased and B_z is suddenly changed outside the operating zone. The measured B_z are marked with "square boxes." The calculated and measured results are in close agreement. Their mean and maximum differences are found to be 1.8% and 6.35%, respectively. The variation of the flux density, $\Delta|B_z|$, found in the experimental prototype is 0.475, satisfying the allowable variation of 0.49 given in Table III. The calculated and measured values of B_z at $z = -20$ mm and $z = 20$ mm are given in the media file.

B. Performance of the WPT System

The output power of the receiver is studied on a constant output resistor. The rectifying circuit is replaced by an output resistor of 46.2 Ω. Fig. 9 shows the output power P_o on $R_{o,mea}$ over *XY* plane at $z = 0$ mm. The results of P_o at $z = -20$ mm and $z = 20$ mm are given in the media file. The calculated and measured results are in close agreement. Their mean and maximum absolute differences are found to be 3.17% and 7.60%, respectively. The error is relatively significant near the boundary of the operating zone due to the abrupt change of the magnetic flux density. The minimum P_o is 173 mW, which can meet the design requirement of 170 mW.

The operation of the diode-bridge rectifier and the LDO is taken into consideration. The output voltage of the diode-bridge rectifier, V_{rect}, is estimated and verified experimentally. Fig. 10 shows the profile of the rectifier voltage V_{rect} on *XY* plane at $z = 0$ mm. The results of V_{rect} at $z = -20$ mm and $z = 20$ mm are given in the media file. The calculated and measured results are in close agreement. Their mean and maximum absolute differences are 2.81% and 6.98%, respectively. $V_{\text{rect,cal}}$ varies between 2.52 and 5.46 V, within the requirement in Table III.

VI. EVALUATION OF SAR

BRs and maximum permissible exposures (MPEs) are recommended in [27] as safety levels to protect human body from adverse heating effects under exposures to electromagnetic fields. The BR of localized exposure for the general public is measured by SAR and is equal to 2 W/kg, which is an averaged value over any 10 g of tissue. Based on the BRs, the MPEs measured by the magnetic field strength are introduced and obtained by mathematical modeling and extrapolation from the experimental results at specific frequencies. It is mentioned in [27] that, in near-field applications, MPEs may not ensure compliance with the BR on local SAR and it may be necessary to directly evaluate the level of local SAR. Therefore, exposures to electromagnetic fields in WPT applications should be directly evaluated by the BRs, i.e., local SAR, instead of MPEs, i.e., the magnetic field strength.

The SAR level in the animal is contributed by the magnetic field generated by the current passing through the transmitting coil and receiving coil. In [36], only the magnetic field of the transmitting coil is studied. However, as the receiving coil is just attached on the animal, they are closely coupled. The SAR level caused by the receiving coil could be relatively significant. The local SAR level with the rat model is simulated by COMSOL Multiphysics [43]. Fig. 11 shows the geometrical setup of the simulation. The dimensions of the transmitting coil and the transmitting coil current are given in Table IV. The dimensions of the receiving coil are given in Table V and the receiving coil

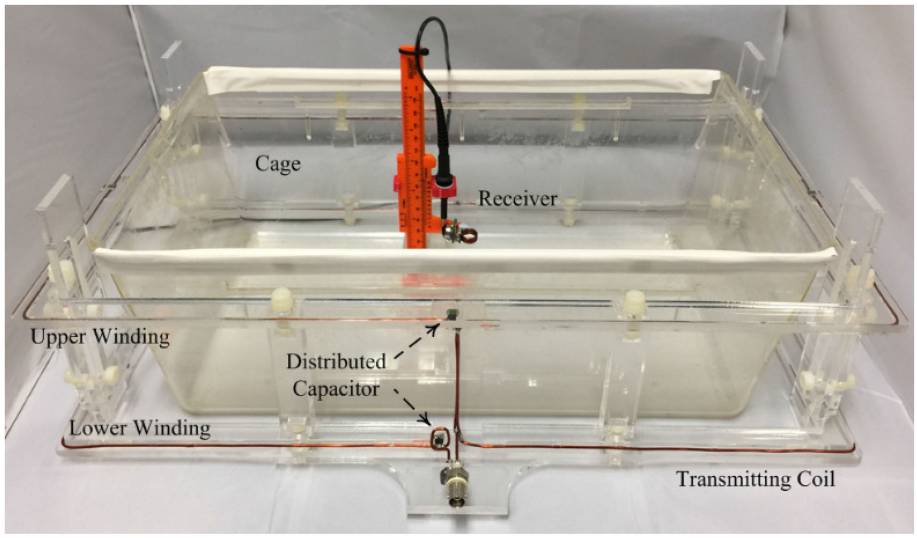

(a)

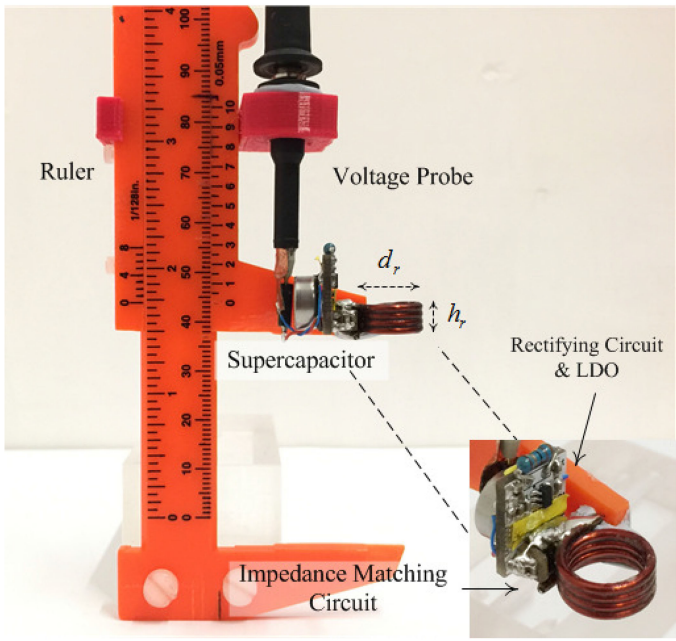

(b)

Fig. 7. Experimental setup. (a) Overall system. (b) Receiver and load.

TABLE III
DESIGN PARAMETERS AND ELECTRONIC COMPONENTS FOR THE WPT SYSTEM

P_L (mW)	V_L (V)	V_{rect} (V)	P_o (mW)	R_o (Ω)	LDO	Diodes
100	1.80	2.5 ~ 5.5	170 ~ 340	45.3 ~ 89.0	LP2985	DB2J20900L

current is determined with the equivalent circuit in Fig. 2. A rat model composed of muscle tissue is used in the simulation, [47]–[48]. The physical parameters and electrical properties of the rat model used in the SAR simulation are summarized in Table VI.

The SAR on the rat model is determined by the maximum averaged value over a 10 g tissue. The maximum averaged SAR at different positions is determined and given in Table VII. The value of SAR is much lower than the BR recommended in [27]. The highest SAR is around one-hundredth of the restriction level when the rat model is located at $x = 150$ mm and $y = –40$ mm. This implies that there is a room for further increasing the transferred power and reducing the size of the receiving coil. Local SAR normalized by the BR in dB value, $\hat{\mathrm{SAR}}$, is defined

TABLE IV
PARAMETERS OF THE TRANSMITTING COIL AND THE OPERATING ZONE USED IN THE EXPERIMENT

C_1 (nF)	L_1 (μH)	r_1 (Ω)	N_1	i_{in} (A)	f (MHz)
0.141	3.91	1.01	1	2.00	6.78
$B_{1A,min}$ (μT)	L_{coil} (mm)	W_{coil} (mm)	H_{coil} (mm)	AR, HR	Wire size
5.68	490	290	95	0.68, 0.42	14 AWG

*C_1 is the equivalent capacitance of the series resonant capacitors distributed over the transmitting coil.

TABLE V
PARAMETERS OF THE RECEIVING COIL AND IMPEDANCE MATCHING CIRCUIT USED IN THE EXPERIMENT

C_{rect} (mF)	C_{21} (nF)	C_{22} (nF)	L_2 (μH)	r_2 (Ω)	N_2
100	3.48	0.13	0.153	0.057	4
B_z (μT)	ΔB_z	d_r (mm)	h_r (mm)	Wire size	Weight (g)*
11.3 ~ 16.8	0.49	11.45	5.80	16 AWG	4.80

*Total weight of the receiver, including the receiving coil, matching capacitors, supercapacitors, LDO, and the load.

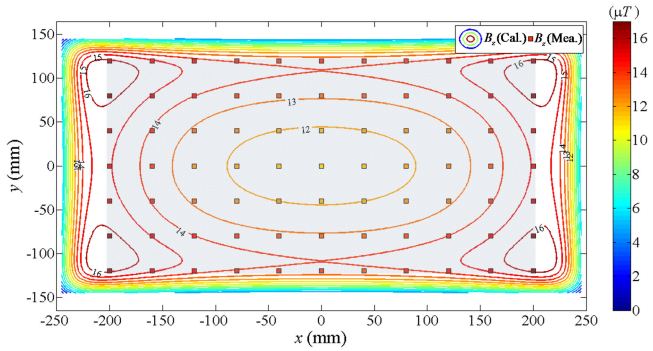

Fig. 8. Calculated and measured B_z at $z = 0$ mm.

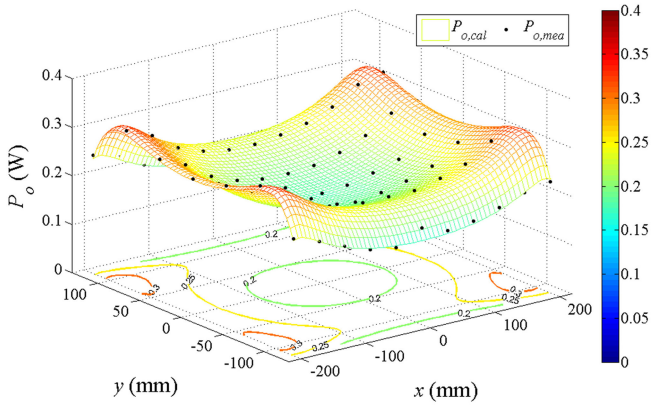

Fig. 9. Calculated and measured P_o on $R_{o,mea}$ at $z = 0$ mm.

as follows:

$$\hat{\mathrm{SAR}} = \log_{10}\left(\frac{\mathrm{SAR_{sim}}}{\mathrm{SAR_{BR}}}\right) \tag{26}$$

where $\mathrm{SAR_{sim}}$ and $\mathrm{SAR_{BR}}$ are the simulated local SAR level and BR, respectively.

A zero value of $\hat{\mathrm{SAR}}$ represents $\mathrm{SAR_{sim}}$ equals the BR. Fig. 12 shows the normalized local SAR located at $x = 150$ mm and $y = –40$ mm. The maximum and minimum $\hat{\mathrm{SAR}}$ are –0.1 and –6.2, respectively. The magnetic flux density distribution in the rat model at the same position is shown in Fig. 13. The distributions viewed at different angles are given in the media file. The maximum and minimum magnetic flux densities are around 187 and 1.37 μT, respectively. For the frequency of 6.78 MHz, MPEs in term of the magnetic flux density [27] equals 3.02 μT. Although the magnetic field exposure is over five times higher than the MPEs as suggested in [27], the averaged SAR over 10 g tissue is much lower than the BR. Thus, evaluation on the local SAR is required.

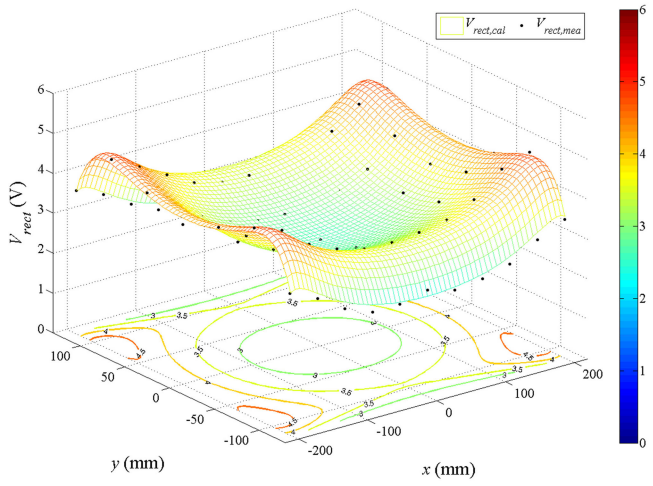

Fig. 10. Calculated and measured V_{rect} at $z = 0$ mm.

VII. DISCUSSIONS

Based on the aforementioned investigations, the following observations are noted.

TABLE VI
PHYSICAL PARAMETERS AND ELECTRICAL PROPERTIES OF THE RAT MODEL

Length (mm)	Width (mm)	Height (mm)	Weight (g)	Density (kg/mm^3)	Relative Permittivity	Electrical Conductivity (S/m)
160	50	70	580	1040	233.27	0.602

TABLE VII
MAXIMUM AVERAGED SAR OVER 10 g OF TISSUE ON THE RAT MODEL

SAR (mW/kg)							
x (mm) / y (mm)	-150	-100	-50	0	50	100	150
40	10.64	9.41	8.91	8.80	9.02	9.69	14.15
-40	12.12	11.16	10.87	10.95	11.47	12.74	15.80

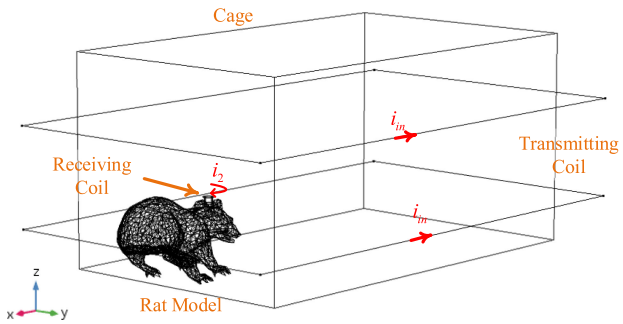

Fig. 11. Geometrical setup of the SAR simulation on the rat model.

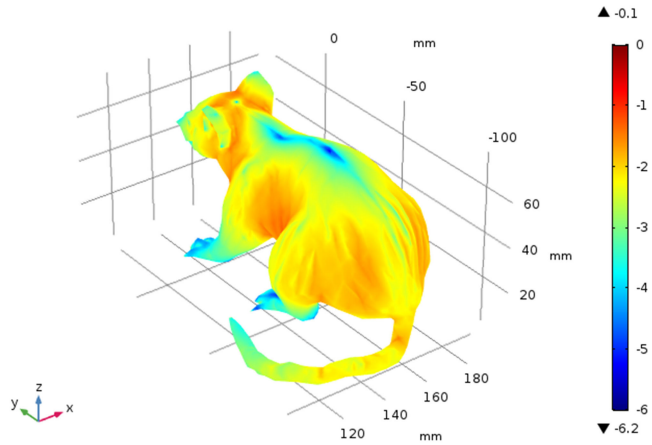

Fig. 12. Normalized local SAR on the rat model in dB value.

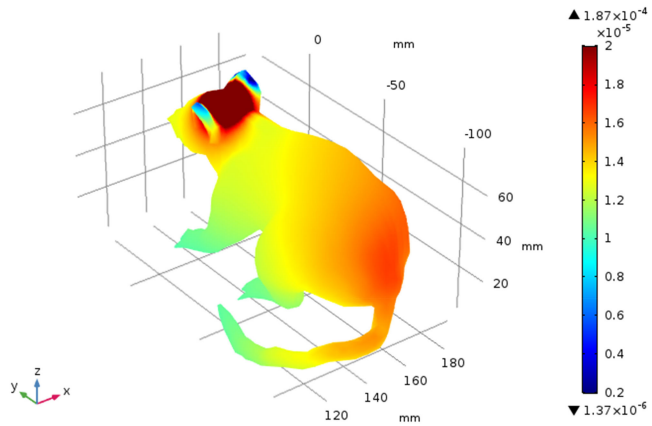

Fig. 13. Magnetic flux density distribution on the rat model.

1) The proposed system does not require dedicated position tracking circuit or wireless communication link. It delivers sufficient and regulated power to the load over a commonly used cage footprint. The transmitting coil is in reasonable dimensions and the receiving coil is relatively small. The SAR level is simulated to be much lower than the BR. Table VIII shows a comparison on the proposed system design with prior art.
2) The steps of designing the dimensions of the transmitting coil are given in Sections III and IV. The magnetic flux density will vary within the design range. The load can still receive sufficient power, even if the receiving coil is located at a location with minimum flux density.
3) The magnetic field flux density can be made more homogeneous in the operating zone by increasing the size, but the excitation current needs to be increased accordingly to achieve the same field strength.
4) Angular misalignments will affect the power transmitted from the transmitter to the receiver. Since the output power to the load is regulated, $V_{\rm rect}$ will decrease as angular misalignment increases. As shown in Fig. 10, without angular misalignment, the minimum value of $V_{\rm rect}$, $V_{\rm rect,min}$, within the operating zone is 2.5 V. As $V_{\rm rect}$ further decreases, the voltage regulation capability of the LDO will be affected. However, as discussed in [32], [49], and [50], the animals have their four limbs mostly stepped on the cage, so the angular misalignment, due to the head shaking and body movement, will not be large. As discussed in [50], the angular misalignment ranges between –25° and +25°. Fig. 14 shows that $V_{\rm rect}$

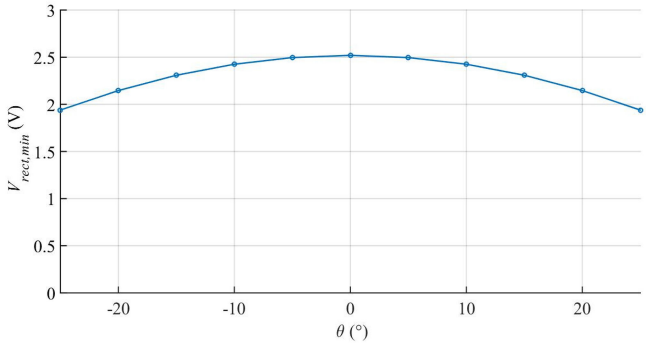

Fig. 14. $V_{\mathrm{rect,min}}$ versus angular misalignment with $i_{\mathrm{in}} = 2$ A.

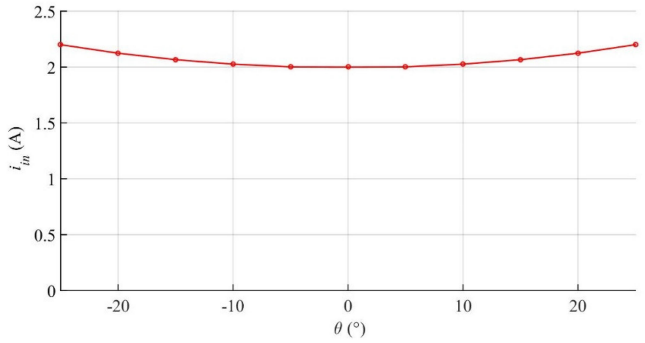

Fig. 15. Required value of i_{in} versus angular misalignment with $V_{\mathrm{rect,min}} = 2.5$ V.

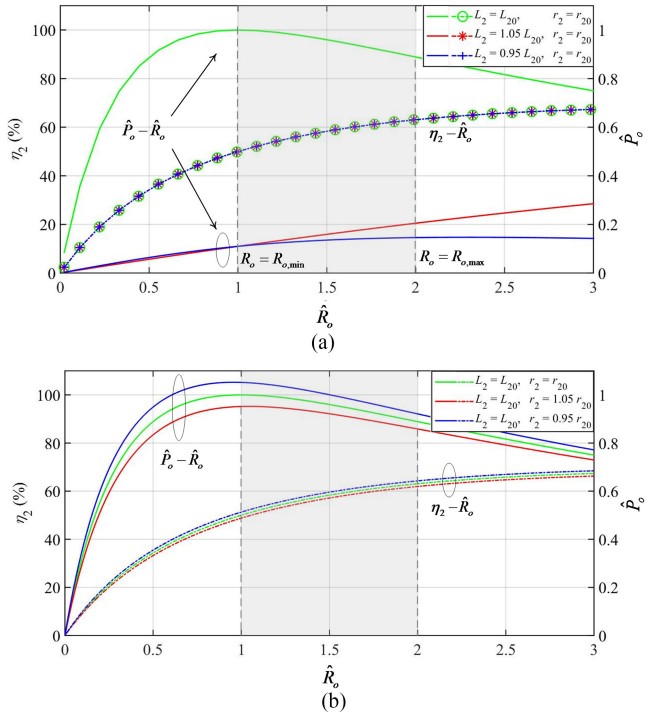

Fig. 16. η_2–$\hat{R}_o$ and $\hat{P}_o$–$\hat{R}_o$ with the same transmitting coil current and matching circuit. (a) Variation of L_2. (b) Variation of r_2.

reduces from 2.5 to 2 V within the aforementioned range of angular misalignment. In order to maintain $V_{\mathrm{rect,min}}$ at 2.5 V, the transmitting coil current i_{in} needs to be increased to 2.2 A. Thus, as illustrated in Fig. 15, the effect of angular misalignment, due the movement of the head of the animal, can be tackled by increasing the transmitting coil current by 10%.

5) Since the designed transmitting coil is placed between the top and bottom of the cage to cover the operating zone of the receiving coil (rat model), the coupling coefficient between the transmitting coil and the receiving coil is larger than that generated by the transmitting coil (or array of coils) placed at the bottom and/or at the top of the cage [8]–[10], [17]–[21]. Regardless of which arrangement of the transmitting coil is used, the required magnetic flux density at the receiving coil should be the same in order to deliver the same load power. However, when the transmitting coils are placed at the bottom and/or the top of the cage, the magnetic flux and its variation around the bottom and/or the top of the cage would be higher than the proposed arrangement [9].
6) The system operates at the maximum power transfer to minimize the SAR in the animal tissues. In Fig. 3, take $\hat{C}_{21} = 0$. At the maximum power transfer condition, $\eta_2 = 50\%$ and $\hat{P}_o = 1.00$. At the maximum efficiency condition, $\eta_2 = 94\%$ and $\hat{P}_o = 0.15$. With the same output power, operating the system at the maximum power transfer condition requires lower transmitting coil current than that at the maximum efficiency condition. It is thus preferable to operate the system at the former condition to minimize the SAR.
7) The impedance matching is crucial in the WPT technology [51]. Fig. 16 shows the normalized output power $\hat{P}_o$ and efficiency η_2 versus $\hat{R}_o$ with the same transmitting coil current and matching circuit. Fig. 16(a) shows the results with the variations of the receiving coil inductance L_2. When L_2 has variation of 5%, η_2 remains almost unchanged but $\hat{P}_o$ decreases. Fig. 16(b) shows the results with the variations of the receiving coil resistance r_2. When r_2 has variation of 5%, η_2 varies less than 2% and $\hat{P}_o$ has variation of 5%. The matching circuit in the prototype achieves a good matching condition. The measured results in Figs. 9 and 10 are in close agreement with the design.
8) The commercially available capacitors can provide sufficient accuracy to achieve good matching condition. The capacitors are of mica type [38]. The matching circuit is designed to receive sufficient power from the transmitter under the worst-case situation, where $R_o = R_{o,\min}$. $R_{o,\min} = 45.3\,\Omega$. The measured output impedance $Z_{\mathrm{IM2,mea}}$ of the matching circuit is measured by HP 4194A and is shown in Fig. 17. The value of Z_{IM2} is equal to $46.1\angle{-0.72}^\circ\ \Omega$. The difference between the matching circuit and the output load is less than 2%. Therefore, the matching circuit can well match the receiving coil with the rectifier circuit.

TABLE VIII
COMPARISON WITH PRIOR ART

	2014 [17]	2015 [9]	2015 [18]	2016 [10]	2017 [23]	This work
Cage footprint (mm^2)	580×610	360×180	300×300	225×225	460×240	400×240
Outer Dimension of Transmitting Coil Set (mm^2/mm^3)	1030×900	540×300	280×80	270×270 ×160	440×240 ×200	490×290 ×95
Outer Dimension of Receiving Coil Set (mm^2/mm^3)	40×40	40×40× 20	25×25	44×44	22×20× 11	11.5×11.5 ×5.8
DC Output Power (mW)	20	215	24	100	40	100
Excitation frequency (MHz)	13.56	1.5	13.56	13.56	13.56	6.78
Wireless communication	Yes	No	Yes	No	Yes	No
Intelligent Checking System	Yes	Yes	Yes	No	No	No
Simulation of SAR in the animal	No	No	No	No	Yes	Yes

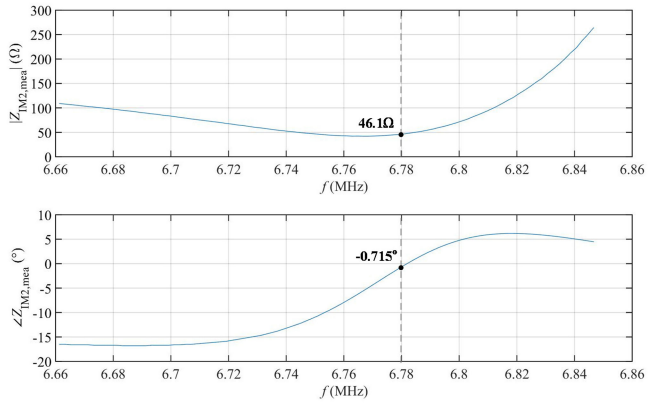

Fig. 17. Measured output impedance $Z_{\mathrm{IM2,mea}}$ of the matching circuit versus frequency.

9) Compared with the multi-coil structures with intelligent control to excite the coil(s) placed under the rat model, the proposed arrangement is not optimized at the maximum power transfer efficiency. However, the power level of electrophysiological applications is usually low (less than 100 mW). Although the power transfer efficiency is between 7.5% and 3.8%, the power loss on the transmitting coil is only around 4 W. The transfer efficiency is not a major concern in this application. Instead, the circuit elegance is the primary consideration. In fact, driving the coils in an intelligent way would cause extra power consumption that might be higher than the power loss of the entire system. For example, a lot of power is consumed on the computer to operate the intelligent tracking system.
10) The optimal circuit configuration for matching the impedance between the receiving coil and the load to achieve maximum power transfer is found to be a shunt-series capacitor network. It can minimize the overall size of the matching circuit and maintain the power efficiency of the receiver over 50%.
11) As the transmitting coil wires wounded around the cage are thin, the coil does not noticeably block the line of sight to observe the behavior and movement of the animal. Such an arrangement has such merit over the one having multiple coils placed on the top of the cage. The proposed system also allows conducting experiments with multiple animals in the cage.
12) Currently, the receiving coil is fixed on the head of the animal and the wireless power is transferred through the air. In the future, the receiving coil with biocompatible packaging is possible to be implanted into the animal's body [52].

VIII. CONCLUSION

A generalized design approach for the WPT system with the transmitting coil made of two rectangular coaxial windings connected in series and wrapped around an animal cage for electrophysiological application has been presented. The generated magnetic flux density with different transmitting coil dimensions and the operating zone has been assessed. An impedance matching circuit in the receiver is designed to maximize output power instead of power transfer efficiency to minimize the transmitting coil current and the SAR. The physical volume of the matching circuit is optimized. A testing prototype has been fabricated. Experimental results have been verified that the WPT system can deliver an output power of 100 mW dc with an 11.45-mm receiving coil in the cage footprint of 400 × 240 mm^2. The SAR is evaluated with finite-element simulation. The highest SAR level is found to be much lower than the limit suggested by the international standards [27]. Moreover, evaluation on the local SAR is required.

APPENDIX

A. Expressions of the Parameters in (15) and (16)

$$k_c = \sqrt{\frac{{d_r}^2}{{d_r}^2 + {\Delta_{ij}}^2}}, k_m = 0.3379\left(1 - \frac{1 - 0.01711}{N_2 - 0.01711}\right)$$

$$+ In(N_2)\left(\frac{-0.16641}{N_2} + \frac{0.00479}{{N_2}^2} + \frac{0.001772}{{N_2}^3}\right)$$

$$k_s = \frac{5}{4} - \mathrm{In}\left(\frac{2d_t}{d_w}\right),\ \Delta_{ij} = \frac{h_r - d_r}{N_2 - 1}|i - j|,\ \delta = \frac{1}{\sqrt{\mu_0 \sigma \pi f}},$$

$$\Phi_{\mathrm{cond}}(x) = Re\left\{\frac{(-1+j)x}{2}\frac{J_0[(-1+j)x]}{J_1[(-1+j)x]}\right\}$$

$$\Phi_{\mathrm{ind}}(x) = Re\left\{jx^2\frac{J_2[(-1+j)x]}{J_1[(-1+j)x]}\right\}, \langle {H_p}^2 \rangle$$

$$= \sum_{i=1}^{N_2}\sum_{j=1}^{N_2}({H_z}^2 + {H_r}^2)(1 - \psi_{ij}), H_z = \frac{K(k_c) - E(k_c)}{2\pi\sqrt{{\Delta_{ij}}^2 + {d_r}^2}}.$$

$$H_r = \frac{\Delta_{ij}}{\pi d_r \sqrt{{\Delta_{ij}}^2 + {d_r}^2}}\left[\frac{2{\Delta_{ij}}^2 + {d_r}^2}{2{\Delta_{ij}}^2}E(k_c) - K(k_c)\right], \psi_{ij} = 1$$

for $(i = j)$, d_r and h_r are the diameter and the height of the receiving coil, respectively, d_t is the diameter of the conducting wire with insulation layer, K and E are the complete elliptic integral of the first and second kind, respectively, σ_{Cu} is the electrical conductivity of copper, $\langle {H_p}^2 \rangle$ is the average of the square field over the turn p^{th} per ampere of current, J_0, J_1, and J_2 are the Bessel functions of the first kind and order 0, 1, and 2, respectively.

B. Expressions of the Parameters in (22a) and (22b)

$$\delta_{11} = \sqrt{\left(\frac{L_{\mathrm{coil}}}{2} + x\right)^2 + \left(y + \frac{W_{\mathrm{coil}}}{2}\right)^2 + \left(z - \frac{H_{\mathrm{coil}}}{2}\right)^2},$$

$$\delta_{12} = \sqrt{\left(\frac{L_{\mathrm{coil}}}{2} - x\right)^2 + \left(y + \frac{W_{\mathrm{coil}}}{2}\right)^2 + \left(z - \frac{H_{\mathrm{coil}}}{2}\right)^2}$$

$$\delta_{13} = \sqrt{\left(\frac{L_{\mathrm{coil}}}{2} - x\right)^2 + \left(y - \frac{W_{\mathrm{coil}}}{2}\right)^2 + \left(z - \frac{H_{\mathrm{coil}}}{2}\right)^2},$$

$$\delta_{14} = \sqrt{\left(\frac{L_{\mathrm{coil}}}{2} + x\right)^2 + \left(y - \frac{W_{\mathrm{coil}}}{2}\right)^2 + \left(z - \frac{H_{\mathrm{coil}}}{2}\right)^2}$$

$$\delta_{21} = \sqrt{\left(\frac{L_{\mathrm{coil}}}{2} + x\right)^2 + \left(y + \frac{W_{\mathrm{coil}}}{2}\right)^2 + \left(z + \frac{H_{\mathrm{coil}}}{2}\right)^2},$$

$$\delta_{22} = \sqrt{\left(\frac{L_{\mathrm{coil}}}{2} - x\right)^2 + \left(y + \frac{W_{\mathrm{coil}}}{2}\right)^2 + \left(z + \frac{H_{\mathrm{coil}}}{2}\right)^2}$$

$$\delta_{23} = \sqrt{\left(\frac{L_{\mathrm{coil}}}{2} - x\right)^2 + \left(y - \frac{W_{\mathrm{coil}}}{2}\right)^2 + \left(z + \frac{H_{\mathrm{coil}}}{2}\right)^2},$$

$$\delta_{24} = \sqrt{\left(\frac{L_{\mathrm{coil}}}{2} + x\right)^2 + \left(y - \frac{W_{\mathrm{coil}}}{2}\right)^2 + \left(z + \frac{H_{\mathrm{coil}}}{2}\right)^2}$$

$$e_1 = \frac{L_{\mathrm{coil}}}{2} + x,\ e_2 = \frac{L_{\mathrm{coil}}}{2} - x,\ e_3 = -\left(\frac{L_{\mathrm{coil}}}{2} - x\right),$$

$$e_4 = -\left(\frac{L_{\mathrm{coil}}}{2} + x\right), g_1 = y + \frac{W_{\mathrm{coil}}}{2},\ g_2 = g_1,$$

$$g_3 = y - \frac{W_{\mathrm{coil}}}{2},\ \text{and}\ g_4 = g_3.$$

REFERENCES

[1] Y. Lin *et al.*, "A battery-less, implantable neuro-electronic interface for studying the mechanisms of deep brain stimulation in rat models," *IEEE Tran. Biomed. Circuits Syst.*, vol. 10, no. 1, pp. 98–112, Mar. 2015.

[2] K. Nowak *et al.*, "Optimizing a rodent model of Parkinson's disease for exploring the effects and mechanisms of deep brain stimulation," *Parkinson's Dis.*, vol. 2011, pp. 1–19, Apr. 2011, doi: 10.4061/2011/414682.

[3] M. A. Lebedev and M. A. L. Nicolelis, "Brain-machine interfaces: Past, present and future," *Trends Neurosci.*, vol. 29, no. 9, pp. 536–546, Jul. 2006.

[4] C. Hamani, M. Diwan, S. Isabella, A. Lozano, and J. N. Nobrega, "Effects of different stimulation parameters on the antidepressant-like response of medial prefrontal cortex deep brain stimulation in rats," *J. Psychiatric Res.*, vol. 44, no. 11, pp. 683–687, Jan. 2010.

[5] A. Aravanis *et al.*, "An optical neural interface: In vivo control of rodent motor cortex with integrated fiberoptic and optogenetic technology," *J. Neural Eng.*, vol. 4, no. 3, pp. 143–156, 2007.

[6] R. Normann, E. Maynard, P. Rousche, and D. Warren, "A neural interface for a cortical vision prosthesis," *Vis. Res.*, vol. 39, no. 15, pp. 2577–2587, 1999.

[7] Q. Wang, H. R. Brunner, and M. Burnier, "Determination of cardiac contractility in awake unsedated mice with a fluid-filled catheter," *Amer. J. Physiol. Heart Circle Physiol.*, vol. 286, no. 2, pp. 806–814, 2004.

[8] U. Jow, M. Kiani, X. Huo, and M. Ghovanloo, "Towards a smart experimental arena for long-term electrophysiology experiments," *IEEE Trans. Biomed. Circuits Syst.*, vol. 6, no. 5, pp. 414–423, Oct. 2012.

[9] N. Soltani, M. S. Aliroteh, M. T. Salam, J. Luis, and P. Velazquez, "Low-radiation cellular inductive powering of rodent wireless brain interfaces: Methodology and design guide," *IEEE Trans. Biomed. Circuits Syst.*, vol. 10, no. 4, pp. 920–932, Aug. 2016.

[10] S. A. Mirbozorgi, H. Bahrami, M. Sawan, and B. Gosselin, "A smart cage with uniform wireless power distribution in 3D for enabling long-term experiments with freely moving animals," *IEEE Trans. Biomed. Circuits Syst.*, vol. 10, no. 2, pp. 424–434, Apr. 2016.

[11] D. Budgett *et al.*, "Novel technology for the provision of power to implantable physiological devices," *J. Appl. Phys.*, vol. 102, no. 4, pp. 1658–1663, 2007.

[12] A. Bagheri *et al.*, "Massively-parallel neuromonitoring and neurostimulation rodent headset with nanotextured flexible microelectrodes," *IEEE Trans. Biomed. Circuits Syst.*, vol. 7, no. 5, pp. 601–609, Oct. 2013.

[13] A. M. Sodagar, G. E. Perlin, Y. Yao, K. Najafi, and K. D. Wise, "An implantable 64-channel wireless microsystem for single-unit neural recording," *IEEE J. Solid-State Circuits*, vol. 44, no. 9, pp. 2591–2604, Sep. 2009.

[14] T. A. Szuts *et al.*, "A wireless multi-channel neural amplifier for freely moving animals," *Nature Neurosci.*, vol. 14, no. 2, pp. 263–269, Feb. 2011.

[15] A. Schwartz, X. Cui, D. Weber, and D. Moran, "Brain-controlled interfaces: Movement restoration with neural prosthetics," *Neuron*, vol. 52, no. 1, pp. 205–220, Oct. 2006.

[16] P. Cong, N. Chaimanonart, W. H. Ko, and D. J. Young, "A wireless and batteryless 10-bit implantable blood pressure sensing microsystem with adaptive RF powering for real-time laboratory mice monitoring," *IEEE J. Solid-State Circuits*, vol. 44, no. 12, pp. 3631–3644, Dec. 2009.

[17] U. Jow, P. McMenamin, M. Kiani, J. R. Manns, and M. Ghovanloo, "EnerCage: A smart experimental arena with scalable architecture for behavioral experiments," *IEEE Trans. Biomed. Eng.*, vol. 61, no. 1, pp. 139–148, Jan. 2014.

[18] B. Lee, M. Kiani, and M. Ghoovanloo, "A smart wirelessly-powered homecage for long-term high-throughput behavioral experiments," *IEEE Sens. J.*, vol. 15, no. 9, pp. 4905–4916, Sep. 2015.

[19] S. Mirbozorgi, H. Bahrami, M. Sawan, and B. Gosselin, "A smart multicoil inductively coupled array for wireless power transmission," *IEEE Trans. Ind. Electron.*, vol. 61, no. 11, pp. 6061–6070, Nov. 2014.

[20] E. Kilinc, G. Conus, C. Weber, B. Kawkabani, F. Maloberti, and C. Dehollain, "A system for wireless power transfer of micro-systems in-vivo implantable in freely moving animals," *IEEE Sens. J.*, vol. 14, no. 2, pp. 522–531, Feb. 2014.
[21] K. Eom *et al.*, "A wireless power transmission system for implantable devices in freely moving rodents," *Med. Biol. Eng. Comput.*, vol. 52, no. 8, pp. 639–651, Aug. 2014.
[22] S. A. Mirbozorgi, Y. Jia, D. Canales, and M. Ghovanloo, "A wirelessly-powered homecage with segmented copper foils and closed-loop power control," *IEEE Trans. Biomed. Circuits Syst.*, vol. 10, no. 5, pp. 979–989, Oct. 2016.
[23] Y. Jia *et al.*, "Position and orientation insensitive wireless power transmission for enercage-homecage system," *IEEE Trans. Biomed. Eng.*, vol. 64, no. 10, pp. 2439–2449, Oct. 2017.
[24] S. C. Tang and N. J. McDannold, "Power loss analysis and comparison of segmented and unsegmented energy coupling coils for wireless energy transfer," *IEEE J. Emerg. Sel. Topics Power Electron*., vol. 3, no. 1, pp. 215–225, Mar. 2015.
[25] Animal Research Review Panel (ARRP) Guideline 20: Guideline for the Housing of Rats in Scientific Institutions, 2007.
[26] S. C. Tang, "A low-operating-voltage wireless intermediate-range scheme for energy and signal transmission by magnetic coupling for implantable devices," *IEEE J. Emerg. Sel. Topics Power Electron.*, vol. 3, no. 1, pp. 242–251, Mar. 2015.
[27] *Standard for Safety Levels With Respect to Human Exposure to Radio Frequency Electromagnetic Fields, 3 kHz to 300 GHz*, IEEE Std C95.1-2005 (Revision of IEEE Std C95.1-1991), 2006.
[28] J. Gordon, "Effects of ambient temperature and exposure to 2450-MHz microwave radiation on evaporative heat loss in the mouse," *J. Microw. Power*, vol. 17, pp. 145–150, 1982.
[29] J. Gordon, "Note: Further evidence of an inverse relation between mammalian body mass and sensitivity to radio-frequency electromagnetic radiation," *J. Microw. Power*, vol. 18, pp. 377–383, 1983.
[30] A. Guy, P. Kramar, C. Harris, and C. Chou, "Long-term 2450-MHz CW microwave irradiation of rabbits: Methodology and evaluation of ocular and physiologic effects," *J. Microw. Power*, vol. 15, pp. 37–44, 1980.
[31] J. Chow, H. Chung, and C. S. Cheng, "Use of transmitter-side electrical information to estimate mutual inductance and regulate receiver-side power in wireless inductive link," *IEEE Trans. Power Electron.*, vol. 31, no. 9, pp. 6079–6091, Feb. 2016.
[32] I. J. Makowska and D. M. Weary, "The importance of burrowing, climbing and standing upright for laboratory rats," *Royal Soc. Open Sci.*, vol. 3, no. 6, pp. 1–12, Jun. 2016.
[33] *MS Lithium Rechargeable Battery*, Seiko Instruments, Inc. [Online]. Available: http://www.sii.co.jp/en/me/battery/products/ms-lithium-2/
[34] J. Chow, N. Chen, H. Chung, and L. Chan, "An investigation into the use of orthogonal winding in loosely-coupled link for improving power transfer efficiency under coil misalignment," *IEEE Trans. Power Electron*, vol. 30, no. 10, pp. 5632–5649, Nov. 2014.
[35] B. H. Choi, E. S. Lee, Y. H. Sohn, G. C. Jang, and C. T. Rim, "Six degrees of freedom mobile inductive power transfer by crossed dipole Tx and Rx coils," *IEEE Trans. Power Electron.*, vol. 31, no. 4, pp. 3252–3272, Apr. 2016.
[36] J. Chow, H. Chung, L. Chan, N. McDannold, and S. C. Tang, "Design of a wireless power transfer system for devices carried by a freely moving animal in cage," in *Proc. IEEE Energy Convers. Congr. Expo.*, Oct. 2017, pp. 4398–4405.
[37] H. S. Choim, "Half-bridge LLC resonant converter design using FSFA-series Fairchild power switch," Fairchild Semiconductor, San Jose, CA, USA, Appl. Note AN-151, 2007.
[38] *Types MC multilayer RF capacitors, Cornell Dubilier Electronics, Datasheet*, 2008. [Online]. Available: http://www.cde.com/resources/catalogs/MC.pdf
[39] X. Li *et al.*, "A wireless magnetic resonance energy transfer system for micro implantable medical sensors," *Sensors*, vol. 12, no. 8, pp. 10292–10308, Jul. 2012.
[40] E. B. Rosa and F. W. Grover, "Formulas and tables for the calculation of mutual and self inductance," *Bull. Bur. Standards*, vol. 8, pp. 1–237, Jan. 1912.
[41] J. Acero, C. Carretero, R. Alonso, and J. M. Burdío, "Quantitative evaluation of induction efficiency in domestic induction heating applications," *IEEE Trans. Magn.*, vol. 49, no. 4, pp. 1382–1389, Apr. 2013.
[42] J. Simpson, J. Lane, and R. Youngquist, "Simple analytic expressions for the magnetic field of a circular current loop," NASA Technical Documents, 2001.
[43] *COMSOL Multiphysics*, 2019. [Online]. Available: http://www.comsol.com
[44] *Lab Products, Inc., Rat Cage*, 2019. [Online]. Available: http://labproductsinc.com/products/conventional-cages/
[45] *American Fancy Rat & Mouse Association, Rat Lab Cage*, 2015. [Online]. Available: http://www.afrma.org/house4mousep2.htm
[46] M. Misakian, "Equations for the magnetic field produced by one or more rectangular loops of wire in the same plane," *J. Res. Nat. Inst. Stand. Technol.*, vol. 105, no. 4, pp. 557–564, Aug. 2000.
[47] C. Gabriel, "Compilation of the dielectric properties of body tissues at RF and microwave frequencies," Radiofrequency Radiation Division, Brooks AFB, San Antonio, TX, USA, Contract AL/OE-TR-1996-0037, 1996.
[48] C. Gabriel, S. Gabriel, and E. Corthout, "The dielectric properties of biological tissues: II. Measurements in the frequency range of 10 Hz to 20 GHz," *Phys. Med. Biol.*, vol. 41, pp. 2251–2269, 1996.
[49] J. N. Crawley, *What's Wrong With My Mouse?: Behavioral Phenotyping of Transgenic and Knockout Mice*, 2nd ed. Hoboken, NJ, USA: Wiley, 2007.
[50] A. F. Meyer, J. Poort, J. O'Keefe, M. Sahani, and J. F. Linden, "An ultra-light head-mounted camera system integrates detailed behavioral monitoring with multichannel electrophysiology in freely moving mice," *bioRxiv*, Apr. 2018.
[51] J. Chow, H. Chung, C. S. Cheng, and W. Wang, "Use of transmitter-side electrical information to estimate system parameters of wireless inductive links," *IEEE Trans. Power Electron.*, vol. 32, no. 9, pp. 7169–7186, Sep. 2017.
[52] K. Silay, C. Dehollain, and M. Declercq, "Inductive power link for a wireless cortical implant with biocompatible packaging," in *Proc. IEEE Sensors*, 2010, pp. 94–98.

Jeff Po-Wa Chow (S'12–M'17) received the B.Eng. (first class honors) and Ph.D. degrees in electronic engineering from the City University of Hong Kong, Kowloon, Hong Kong, in 2012 and 2017, respectively.

From April to October 2016, he was a Research Trainee with Brigham and Women's Hospital, Harvard Medical School, Boston, MA, USA. From May 2017 to September 2018, he was an Engineer with the Department of Electronic Engineering, City University of Hong Kong. He is currently a Senior Engineer with Huawei Technologies Co., Ltd., Shenzhen, China. He has authored or coauthored more than ten technical papers and filed three patents. His current research interests include wireless power transfer, power factor correction, active electromagnetic interference filter, LEDs driver, photovoltaic systems, and computational intelligence for power electronic systems.

Dr. Chow was the recipient of the First Prize Oral Paper Award and the Best Paper Award from the High-Performance and Emerging Technologies Technical Committee of the IEEE Power Electronics Society in IEEE Energy Conversion Congress and Exposition 2015 and 2017, respectively. He was the recipient of the Outstanding Presentation Award in IEEE Applied Power Electronics Conference 2016.

Henry Shu-Hung Chung (M'95–SM'03–F'16) received the B.Eng. and Ph.D. degrees in electrical engineering from Hong Kong Polytechnic University, Kowloon, Hong Kong, in 1991 and 1994, respectively.

Since 1995, he has been with the City University of Hong Kong, Kowloon, where he is currently a Professor with the Department of Electronic Engineering and the Director of the Center for Smart Energy Conversion and Utilization Research. He has edited one book, authored eight research book chapters, and over 450 technical papers, including 200 refereed journal papers in his research areas, and holds 50 patents. His current research interests include renewable energy conversion technologies, lighting technologies, smart grid technologies, and computational intelligence for power electronic systems.

Dr. Chung was an Editor-in-Chief for IEEE POWER ELECTRONICS LETTERS in 2014–2018 and the Chair of the Technical Committee of the High-Performance and Emerging Technologies, IEEE Power Electronics Society, in 2010–2014. He is currently an Associate Editor for the IEEE TRANSACTIONS ON POWER ELECTRONICS and the IEEE JOURNAL OF EMERGING AND SELECTED TOPICS IN POWER ELECTRONICS. He has received numerous industrial awards for his invented energy saving technologies.

Leanne Lai-Hang Chan (S'07–SM'17) received the B.Eng. degree in electrical and electronic engineering from the University of Hong Kong, Lung Fu Shan, Hong Kong, and the M.S. degree in electronic engineering and the Ph.D. degree in biomedical engineering from the University of Southern California, Los Angeles, CA, USA.

She has been an Associate Professor in electronic engineering with the City University of Hong Kong, Kowloon, Hong Kong. Her research interests include retinal prosthesis, electrical stimulation of retinal, neural recording, implantable electronic system, and computer vision.

Dr. Chan is currently an Associate Editor for the IEEE TRANSACTIONS ON BIOMEDICAL CIRCUITS AND SYSTEMS.

Ruihua Shen received the B.Eng. degree in electrical engineering from Shan Dong University, Jinan, China, in 2017, and is currently working toward the Ph.D. degree in electronic engineering at the City University of Hong Kong, Kowloon, Hong Kong.

Her research interests include nonlinear phenomena analysis of power electronics, pulsewidth modulation technique, and wireless power transfer.

Sai Chun Tang (S'97–M'01–SM'11) was born in Hong Kong in 1972. He received the B.Eng. degree (with first class honors) and the Ph.D. degree in electronic engineering from the City University of Hong Kong, Kowloon, Hong Kong, in 1997 and 2000, respectively.

He was a Research Fellow with the City University of Hong Kong after he graduated. He joined the National University of Ireland, Galway, as a Visiting Academic in 2001, and then the Laboratory for Electromagnetic and Electronic Systems, Massachusetts Institute of Technology, Cambridge, MA, USA, in 2002. In 2004, he joined the Radiology Department, Brigham and Women's Hospital, Harvard Medical School, Boston, MA, USA, for the development of ultrasound diagnosis devices and noninvasive treatment systems using high-intensity focused ultrasound. In 2008, he became a Faculty of Radiology with Harvard Medical School. His current research interests include wireless power transfer, electronic medical devices, high-frequency electromagnetism, low-profile power converter design, and analog electronics.

Dr. Tang was a recipient of Faculty Career Development Award from Harvard Medical School, in 2015, and the First Place Prize Paper Award in IEEE TRANSACTIONS ON POWER ELECTRONICS, in 2017.